International Journal of Fatigue 163 (2022) 107045

Contents lists available at ScienceDirect

International Journal of Fatigue

journal homepage: www.elsevier.com/locate/ijfatigue

Quantifying lamellar microstructural effect on the fatigue performance of bimodal Ti-6Al-4V with microdefect

Keke Tang [a,*], Kunrong Chen [a], Paolo Ferro [b], Filippo Berto [c]

[a] School of Aerospace Engineering and Applied Mechanics, Tongji University, Shanghai 200092, China
[b] University of Padova, Department of Engineering and Management, Stradella San Nicola 3, 36100 Vicenza, Italy
[c] NTNU, Department of Mechanical and Industrial Engineering, Richard Birkelands vei 2b, 7491 Trondheim, Norway

ARTICLE INFO

Keywords:
Bimodal Ti-6Al-4V
Lamellar microstructural effect
Microdefect
Fatigue performance
ADI

ABSTRACT

Fatigue performance of metal alloys is inseparably associated with heterogenous microstructure and existing microdefects. The coordinated effects of lamellar microstructure (LM) and microdefect on fatigue performance of bimodal Ti-6Al-4V is studied within the framework of CPFEM. We propose an intragrain weight integration approach able to account for intragranular accumulative deformation. Parametric accumulative difference indicator (ADI) for stress is defined to relatively quantify the lamellar microstructural effect, overcoming the limitations of experimental procedures. The results demonstrate that the increase of β lath and synchronized refinement of LM appreciably improve lamellar microstructural effect. These attributes can be applied to the material design and manufacturing of advanced metal alloys.

1. Introduction

Microstructures of metal alloys have substantial impact on their mechanical properties such as fatigue performance [1,2], as reflected by the popularity of titanium alloys [3–5]. Generally, there are three categorized groups for titanium alloys, namely α, β and α-β alloys. Tailoring microstructures gives rise to a variety of titanium alloys with distinctive mechanical properties. Deliberate composition of different phases of α and β results in desirable titanium alloys. One of the most popular candidates is Ti-6Al-4V that comprises both hexagonal closed packed (HCP) α phase and body-centered cubic (BCC) β phases. Typical microstructures of Ti-6Al-4V are described as equiaxed, fully lamellar and bimodal [6]. These microstructures can be forged after different heating processes to achieve distinctive microstructural features. The noteworthy bimodal microstructure consists of equiaxed primary α grains and lamellar colonies with secondary α embedded as laths within β grains, providing superior fatigue crack resistance at different developmental stages. Nevertheless, the underlying mechanism of lamellar microstructural effect on the role of fatigue behaviors in bimodal Ti-6Al-4V is rather complex and challenging.

Under fatigue loading, crack initiation is predominantly caused by slip irreversibility. Persistent slip bands (PSB) are formed due to the cyclic loading, in the shape of thin lamellae in localized grains. Constant cyclic loading results in accumulated plastic strain, further leading to the formation of small extrusions and protrusions caused by slip incompatibility with neighboring grains [7]. More intriguingly, accumulated plastic strain in LM is heavily influenced by the colonies and exhibits disparate fatigue resistance performance at the stages of crack initiation and propagation [2]. Considering the inevitable defects such as micro-notches or non-metallic inclusions in metal alloys [8–13], they are rather sensitive to fatigue-related mechanical behaviors. Combination of LM and microdefects in bimodal Ti-6Al-4V poses a grave challenge to fatigue properties in materials and structures.

Previous study [2] indicates that LM has relatively superior fatigue crack propagation resistance, while the primary α phase is considered to have better performance of fatigue crack initiation resistance. In this regard, bimodal Ti-6Al-4V can be tailored to have certain composition of primary α phase and LM, such that the optimal mechanical properties are obtained. Wu et al. [2] performed systematic evaluation of the fatigue strength of Ti-6Al-4V with regard to its three distinctive microstructures of equiaxed, lamellar and bimodal, and concluded that fatigue strength increases in the order of equiaxed, lamellar and bimodal microstructures. However, it is also pointed out that even fatigue strength of bimodal microstructure is improved, further study is required for a final conclusion. Complexity and uncertainties of the challenge is also comprehensively elaborated in the experimental investigation on bimodal and fully lamellar structures by Nalla et al. [14]. The

* Corresponding author.
E-mail address: kktang@tongji.edu.cn (K. Tang).

https://doi.org/10.1016/j.ijfatigue.2022.107045
Received 15 April 2022; Received in revised form 16 May 2022; Accepted 29 May 2022
Available online 2 June 2022

Nomenclature

F	total deformation gradient
F_e	elastic deformation gradient
F_p	plastic deformation gradient
L_p	plastic velocity gradient
$\dot{\gamma}_\alpha$	plastic slip rate on the αth slip system
s^α	slip direction vector of the αth slip system in current configuration
m^α	slip normal plane vector of the αth slip system in current configuration
s_0^α	slip direction vector of the αth slip system in reference configuration
m_0^α	slip normal plane vector of the αth slip system in reference configuration
τ^α	resolved shear stress on the αth slip system
g^α	critical shear stress
n	strain rate sensitive exponent
$\dot{a}$	reference shear strain rate
σ	Cauchy stress tensor
$h_{\alpha\beta}$	hardening modulus matrix
h_0	initial hardening modulus
τ_0	yield shear stress
τ_s	saturated flow stress
$q_{\alpha\beta}$	hardening constant
γ	cumulative shear strain
ψ	weight function
m	constant in weight function
k	linear slope in weight function
r	float variable
$\hbar$	updated weight function
$\Re$	value along the intragranular path
R	weighted cumulative integration for designated grain
δ	accumulative difference indicator

Abbreviations

ADI	Accumulative difference indicator
BCC	Body-centered cubic
BOR	Burgers orientation relationship
CPFEM	Crystal plasticity finite element method
FCG	Fatigue crack growth
HCF	High-cycle fatigue
HCP	Hexagonal closed packed
LM	Lamellar microstructure
PSB	Persistent slip bands
RVE	Representative volume element
VT	Voronoi tessellation

experimental observation for standard bimodal microstructure is compared with a fully lamellar β-annealed microstructure in Ti-6Al-4V under the condition of high cycle fatigue (HCF). Conclusions for the microstructural difference is varied even over the change of loading conditions from pure mode I to mixed-mode loading. Conclusively, extensive literatures are primarily focused on the role of microstructure in influencing the fatigue behaviors of titanium alloys [15–18], with emphasis laid on the arrangement of α and β phases. Considerable effort has been noticeably devoted to highlighting the lamellar microstructural effect in bimodal titanium alloys.

Recent experimental [17–26] and numerical [27–29] progress on titanium alloys with LM are comprehensively reported. The experimental approach is able to capture the actual influence of LM on the mechanical properties of materials, thus is considered to be reliable for microstructural analysis [30]. For instance, Jadhav et al. [17] studied the HCF properties of bimodal Ti-6Al-4V, focusing on the effect of volume fraction of α and transformed β phases. It is indicated that fatigue crack initiation occurs in lamellar grains, these lamellar grains are considered to be softer than α grains due to alloy partitioning effect. It is noteworthy in [21] that influence of microstructure on fatigue crack growth (FCG) behavior of Ti-6Al-3Nb-2Zr-1Mo alloy is studied. Bimodal microstructure and fully LM are respectively investigated for low cycle fatigue behaviors. It is found that the FCG rate of LM is slower than that of bimodal structure. Interpretations on this are proposed by researchers [31], that size of α colony can be regarded as the effective microstructural factor that affects FCG rate. The above results are focused on the stages of fatigue crack initiation and growth, respectively, for varied bimodal titanium alloys. Other mechanical properties such as impact toughness of TC21 alloy with various microstructures is studied in [23], it is experimentally concluded that thick lamellar structure existing in bimodal or fully lamellar structures results in large plastic deformation, and promote crack initiation energy. Up to now, there are extensive experimental researches concerning lamellar microstructural effect in bimodal titanium alloys, which is diversely reflected by the aforementioned literatures in terms of HCF/LCF and impact loading conditions.

Despite the fact that experimental results are direct manifestation of mechanical properties of materials, uncertainties and cost through the exhaustive experimental process cannot be neglected. In contrast, numerically quantifying microstructural attributes tends to be a promising alternative strategy to lower experimental cost and to tailor desirable microstructure [32–35]. Numerical investigations into LM are primarily carried out within the framework of crystal plasticity finite element method (CPFEM). Through CPFEM, explicitly acquired is the accumulated plastic strain at grain scale, and the micromechanical response of representative volume element (RVE) is achieved at mesoscale, providing reference for the efficient design of tailor-made materials at macroscale [36–43]. Although CPFEM is a microstructure-sensitive physics-based tool that is commonly applied to model plasticity and fatigue damage in polycrystalline materials, numerical research on LM in bimodal titanium alloys is rather surprising. To name a few, Zhang et al. [27] studied the microstructural effect on HCF properties of bimodal titanium alloys, through the combined CPFE simulation and extreme value statistics. It is noticed that duplex microstructure models with LM is studied, a lamellae width is adopted as one of the microstructural features. Strain localization complicated by LM during primary hot working of TA15 is addressed in [28], within the numerical framework of a two-scale crystal plasticity model. Mechanism of strain localization is revealed particularly for LM. It is noteworthy a crystal plasticity model is formulated for creep in titanium alloys with fully LM in [43], and can be further applied to a variety of crystalline materials with LM under creep loading. Functionally graded bimodal Ti-6Al-4V with LM are studied through CPFEM in [44], emphasizing the influence of lath thickness from microstructural viewpoint. It shall be pointed out that the microdefect and fatigue loading are not considered in the CPFE modelling on functionally graded bimodal Ti-6Al-4V. Thermal interface grooving and anisotropic deformation of titanium alloy with lamellar colony is also discussed within a modified CPFEM framework in [45]. Though considerable efforts are being devoted to the influence of microdefect on fatigue behaviors in metal alloys, such as varied microdefects in 316L stainless steel [46], notched specimen for aluminum alloy 7075 [47], inclusions in nickel-based superalloys [48], notches in Ti-6Al-4V [49]. Even more elaborated is the effect of defect size and shape on HCF behavior of 316L austenitic steel in [50]. Experiments on microdefect effect in metal alloys are also commonly practiced [51,52]. Nevertheless, to the best of the authors knowledge, the coordinated role of microdefect in bimodal Ti-6Al-4V with LM has

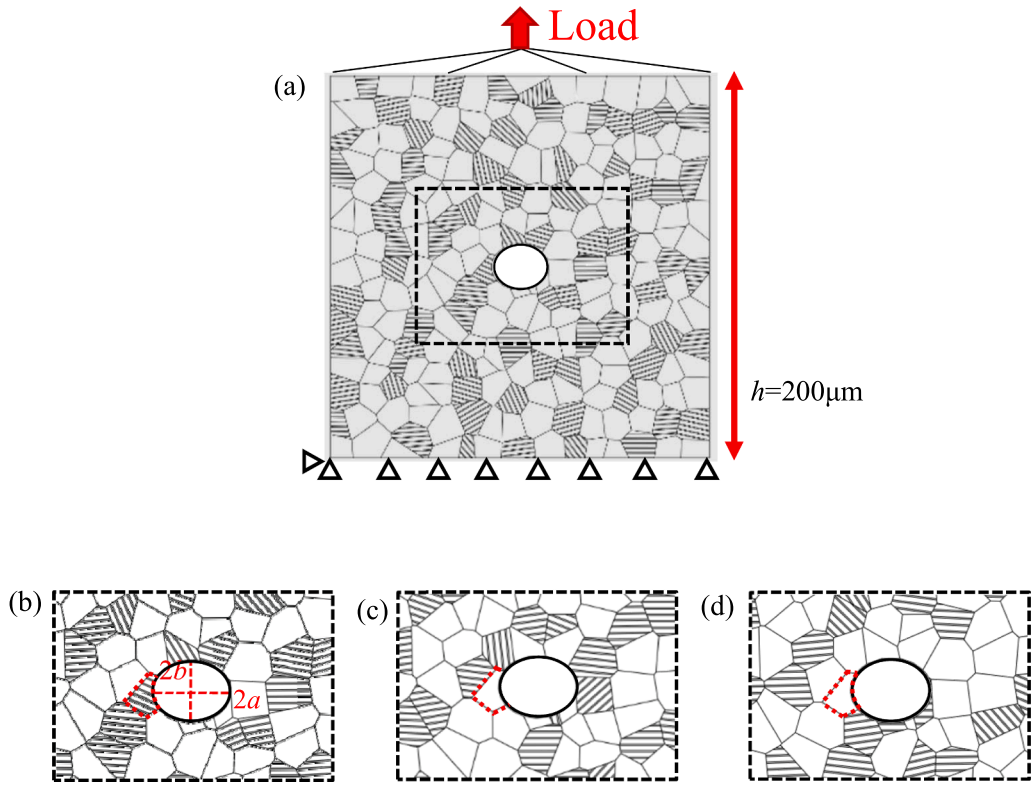

Fig. 1. RVEs for Ti-6Al-4V with elliptical notches: (a) RVE model with boundary condition at the bottom, as well as applied cyclic load at the upper boundary; (b) Case 1 grain with LM distribution on the left edge of elliptical notches (c) Case 2 grain without LM distribution on the left edge of elliptical notches (d) Case 3 Similar to Case 2 but with different general LM distribution.

not been brought into proper focus.

The main goal of the present work is to investigate lamellar microstructural effect on the fatigue performance of bimodal Ti-6Al-4V with designated microdefect, within the framework of CPFEM [53], aiming to propose a weighted accumulative deformation within individual grains and relatively quantify the LM effect on fatigue properties of bimodal titanium alloys. Influence of microdefect size and lamellae width on fatigue performance of the bimodal Ti-6Al-4V is particularly addressed. We start Section 2 with the methodology consisting of RVE modelling and the proposed concept of weighted accumulative deformation, followed by detailed results and discussions in Section 3. Concluding remarks are summarized in Section 4.

2. Methodology

2.1. Crystal plasticity constitutive formulations for Ti-6Al-4V modelling

Herein we adopt a classic crystal plasticity constitutive equation [54] to describe the total deformation consisting of both elastic and plastic deformation. The total deformation gradient F is presented as:

$$F = F_e \bullet F_p \tag{1}$$

Here F_e is the elastic deformation gradient and it is related to the elastic distortion of lattice, F_p is the plastic deformation gradient denoting the plastic shear of crystalline material. Plastic deformation caused by the crystalline slip is related to dislocation motion. L_p is taken as the plastic velocity gradient corresponding to the plastic slip rate $\dot{\gamma}_\alpha$ on the αth slip system.

$$L_p = \dot{F}_p (F_p)^{-1} = \sum_\alpha \dot{\gamma}_\alpha s_0^\alpha \otimes m_0^\alpha \tag{2}$$

It is noted here that unit vectors s_0^α and m_0^α are, respectively, the slip direction and slip plane normal direction for the αth slip system in reference configuration. $\dot{\gamma}_\alpha$ is the plastic shear rate as follows [55]:

$$\dot{\gamma}_\alpha = \dot{a}\left(\frac{\tau^\alpha}{g^\alpha}\right)\left|\frac{\tau^\alpha}{g^\alpha}\right|^{n-1} \tag{3}$$

It is noted that $\dot{a}$ is the reference shear strain rate, g^α is the critical shear stress indicating strength of the αth slip system, n is the strain rate sensitive exponent. τ^α is taken as the resolved shear stress on the αth slip system, it is related to the deformation and Cauchy stress tensor σ as follows:

$$\tau^\alpha = \sigma : (s^\alpha \otimes m^\alpha) \tag{4}$$

It is noted that unit vectors s^α and m^α are, respectively, the slip direction and slip plane normal direction for the αth slip system in current configuration. Slip direction and slip plane normal direction for the αth slip system in reference and current configurations are connected through the following expression:

$$\begin{cases} s^\alpha = F_e \bullet s_0^\alpha \\ m^\alpha = m_0^\alpha \bullet F_e^{-1} \end{cases} \tag{5}$$

The critical shear stress g^α is related to all the active slip systems. Strain hardening law is described as [56]:

$$\dot{g}^\alpha = \sum_\beta h_{\alpha\beta}\dot{\gamma}_\beta \tag{6}$$

Here $h_{\alpha\beta}$ is the matrix of slip hardening modulus, the subscripts α and β are the indices of slip system. If $\alpha = \beta$, $h_{\alpha\beta}$ turns into $h_{\alpha\alpha}$ that is the part of self-hardening, while $h_{\alpha\beta}(\alpha \neq \beta)$ denotes the part of latent hardening. Therefore, $h_{\alpha\beta}$ is expressed as:

Table 1
CPFEM modeling parameters for Ti-6Al-4V [27,37,40].

Parameter	$\dot{\gamma}_0$	n	τ_0/MPa		τ_s/MPa	h_0/MPa	C11 /MPa	C12 /MPa	C44 /MPa	C13 /MPa	C33 /MPa
α(HCP)	0.001	15	Basal	420	462	631.2	162,400	92,000	49,700	69,000	180,700
			Prismatic	370	407	436.2					
			Pyramidal	490	539	436.2					
β(BCC)	0.001	15	333		366	100	135,000	113,000	54,900	–	–

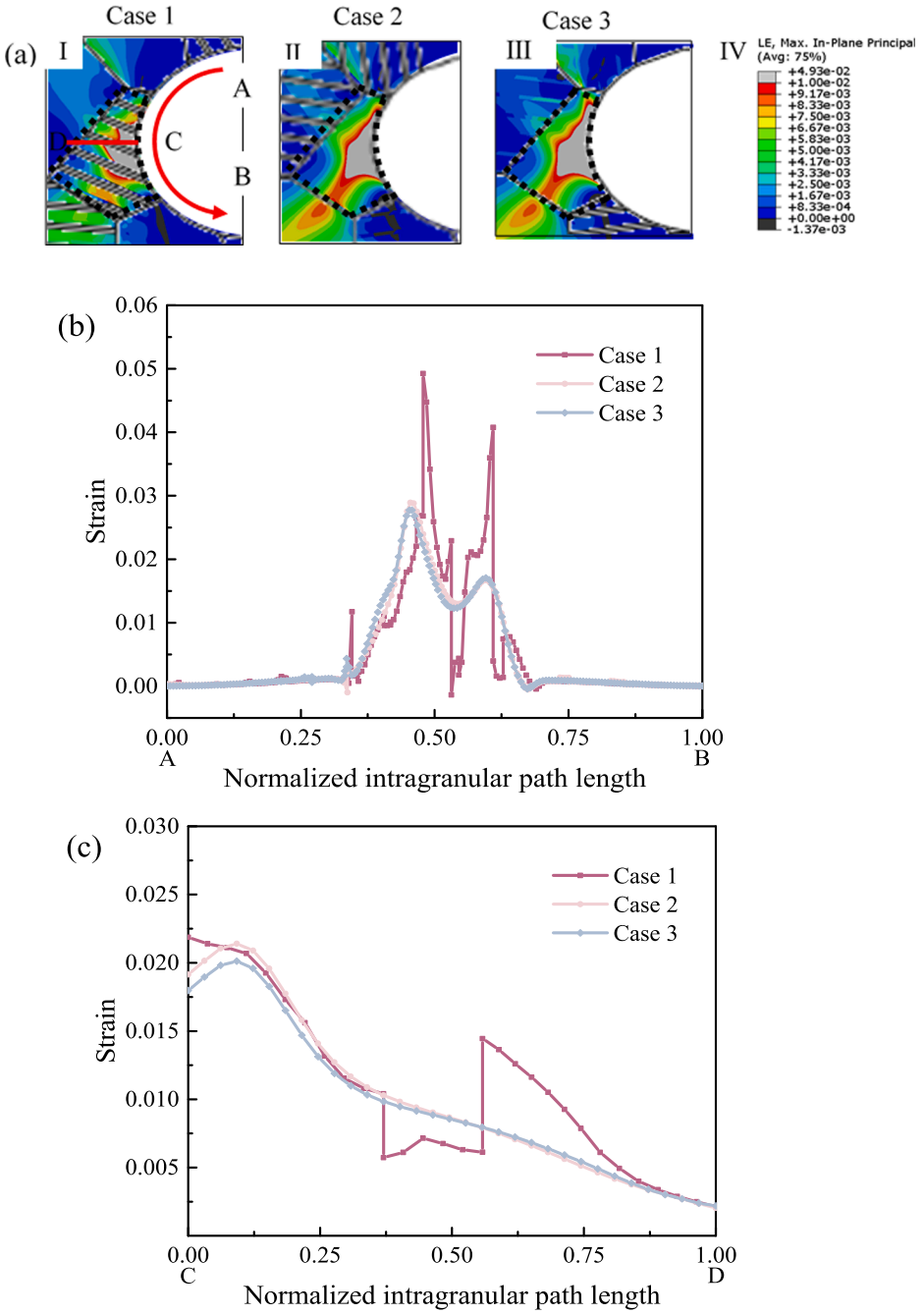

Fig. 2. Strain distribution for three cases (a) Contour plot; (b) Strain distribution along circular path length AB; (c) Strain distribution along intragranular path length CD.

$$\begin{cases} h_{\alpha\alpha} = h_0 \mathrm{sech}^2\left(\dfrac{h_0\gamma}{\tau_0 - \tau_s}\right) \\ h_{\alpha\beta} = q_{\alpha\beta} h_{\beta\beta} (\alpha \neq \beta) \end{cases} \tag{7}$$

Note h_0 is the initial hardening modulus, $q_{\alpha\beta}$ is the hardening constant, τ_0 is the yield shear stress that equals the initial value of g^α, τ_s is the saturated flow stress controlling the limit of g^α. The sum cumulative slip on all slip systems is denoted as γ expressed as follows:

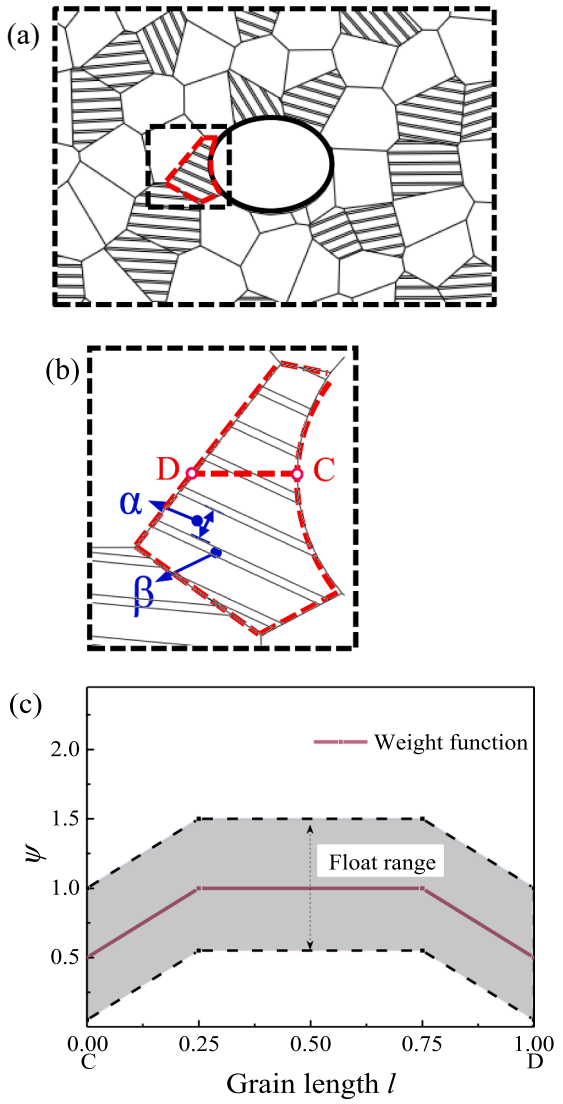

Fig. 3. Intragrain weight integration approach; (a) Designated LM grain neighboring microdefect; (b) Enlarged view of grain with LM; (c) Proposed weight function.

$$\gamma = \sum_{\alpha} \int_0^t \left|\dot{\gamma}_\alpha\right| \mathrm{d}t \tag{8}$$

It shall be emphasized that the crystal plasticity formulations above is implemented in ABAQUS/Standard finite element software as a user material subroutine (UMAT) [53]. The CPFEM framework has been proved to be an effective approach for modeling local response of single or polycrystals at microstructural scale. We further modified it to accommodate bimodal titanium alloys.

2.2. RVE modelling of bimodal Ti-6Al-4V with LM

Bimodal Ti-6Al-4V polycrystalline models with lamellar microstructural features are established through Voronoi tessellation (VT) technique, providing designated representative volume element (RVE) samples. Frist, Random seeds are adopted to generate Voronoi polyhedral. Grain homogenization is further performed in order to avoid short edges and sharp corners. One single RVE is 200 μm*200 μm in dimension and consists of 225 grains with average grain size of 15 μm. There is an elliptical notch prefabricated in the center of RVE, with the dimension of 2*a* and 2*b*, refer to Fig. 1. In order to quantitatively investigate the lamellar microstructural effects, the volume fraction of α

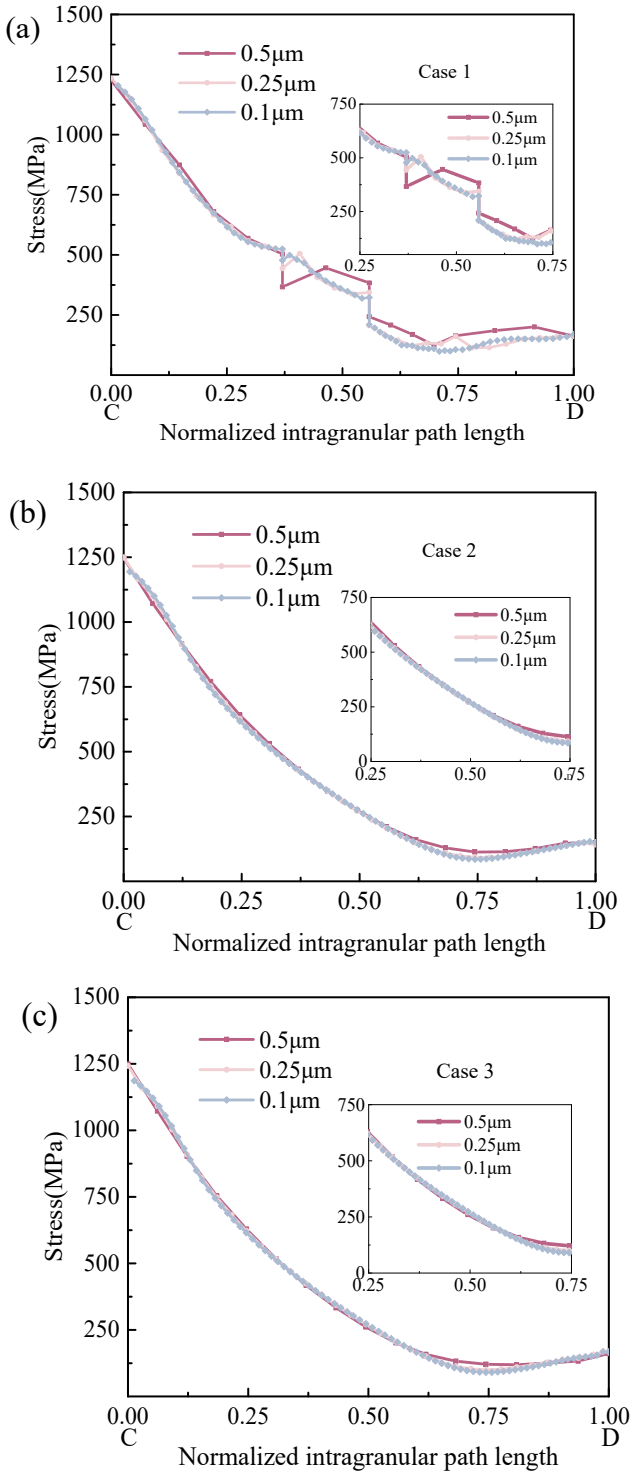

Fig. 4. Intragranular stress distribution for mesh sizes of 0.5 μm, 0.25 μm, and 0.1 μm; (a) Case 1 grain with LM; (b) Case 2 grain without LM; (c) Case 3 grain without LM.

phase is set to be 66% and the volume fraction of LM remains to be 34%. It shall be noticed that the orientation between the α and β phases in LM follows a Burgers orientation relationship (BOR) as reported in [58]. Note the LM in bimodal Ti-6Al-4V is explicitly established within single grain. The thickness of α lath and β lath in the colony is adopted as 2 μm and 0.5 μm, respectively, based on published investigations [37].

It shall be emphasized here that our goal is to relatively quantify the lamellar microstructural effect on the fatigue performance of bimodal

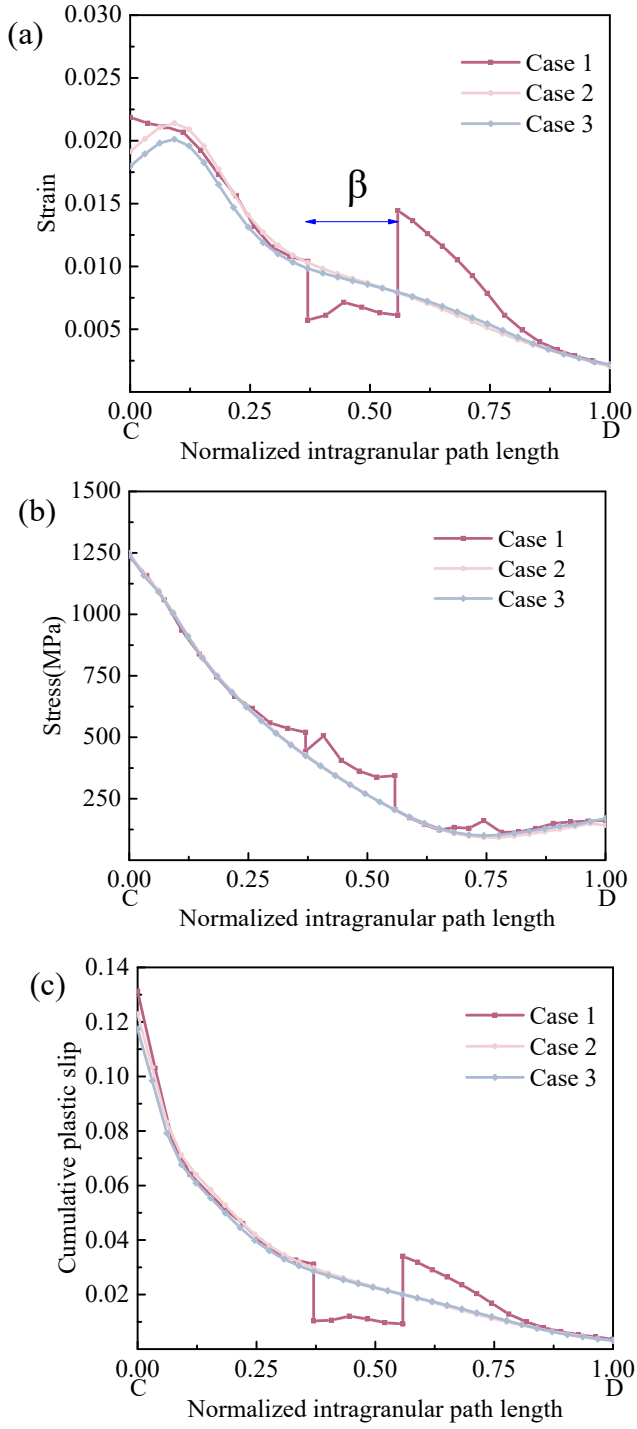

Fig. 5. Intragranular strain/stress/cumulative plastic slip; (a) strain; (b) stress; (c) cumulative plastic slip.

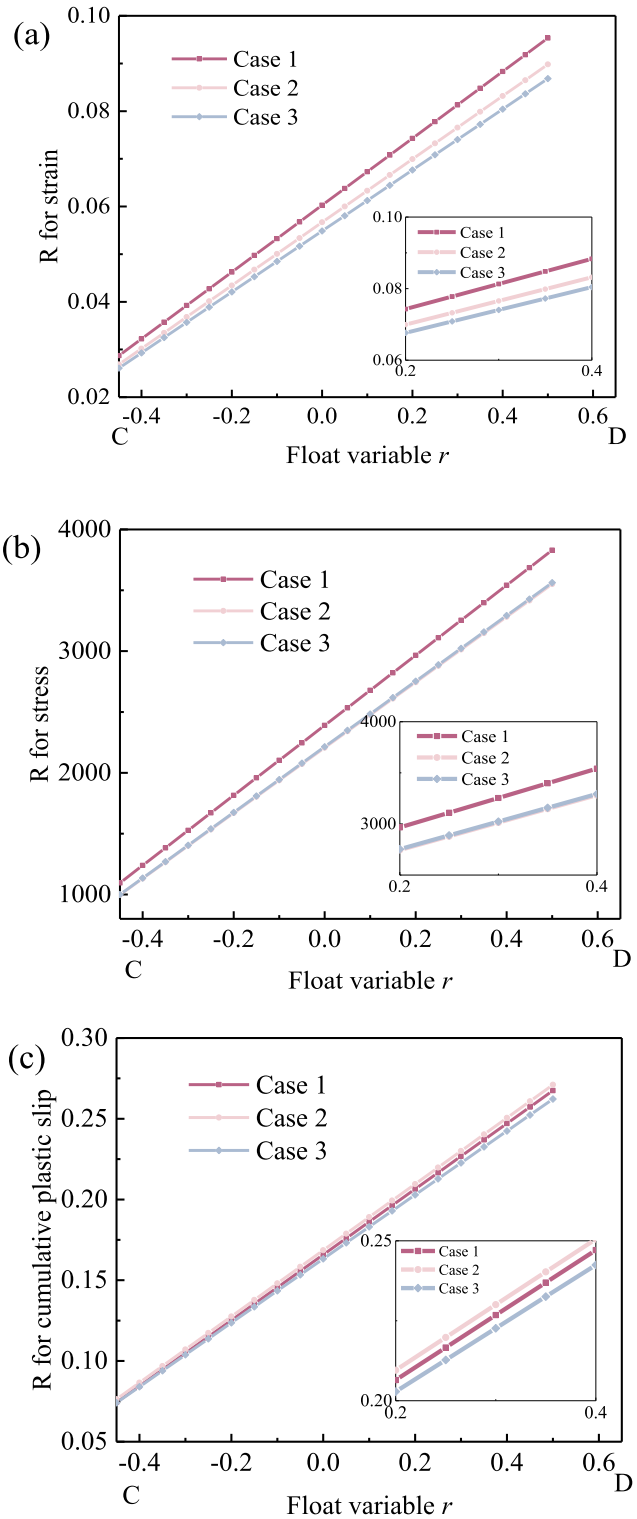

Fig. 6. R for intragranular strain/stress/cumulative plastic slip; (a) R for strain; (b) R for stress; (c) R for cumulative plastic slip.

Ti-6Al-4V. Thus, it is understandable to focus on the neighboring area of elliptical notches where crack initiation most likely emerges. Tailoring the distribution of LM is challenging for experimental procedure but feasible in numerical modelling. In this regard, three typical samples of different LM distributions are designated, as graphically displayed in Fig. 1. Fig. 1(a) displays the complete RVE model with the boundary condition and applied load. It shall be noted that the corner node at the left of boundary is constrained in the direction of both X and Y in order to constrain movement, and other nodes along the bottom boundary are fixed in the Y direction, as depicted in Fig. 1(a). Cyclic sinusoidal loading for fatigue is uniformly applied at the upper boundary, with the maximum tensile stress of 800 MPa and stress ratio R of 0, refer to Fig. 1 (a). Considering computational cost, 10 cycles of loading is carried out.

Basically, the difference among the three specific RVEs is the designated LM distribution. In Fig. 1(b), one grain with LM is designated at the left edge of elliptical notch, as enclosed in red line, while no LM appears on the right edge of the elliptical notch. In Fig. 1(c) and 1(d), no LM is designated on the left edge, while the overall spatial distribution of LM is randomly varied in the RVE model. The purpose of tailoring LM

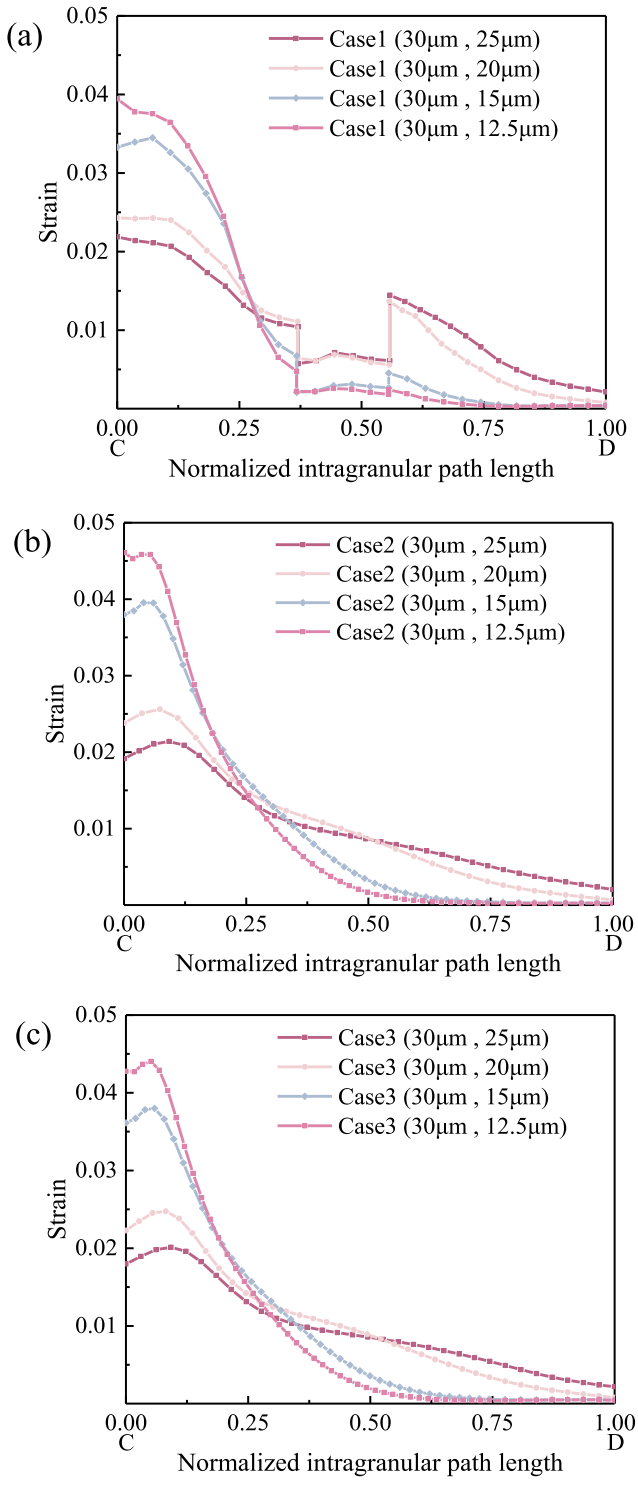

Fig. 7. Strain distribution along intragranular path (a) Case 1 with different aspect ratios; (b) Cases 2 with different aspect ratios; (c) Cases 3 with different aspect ratios.

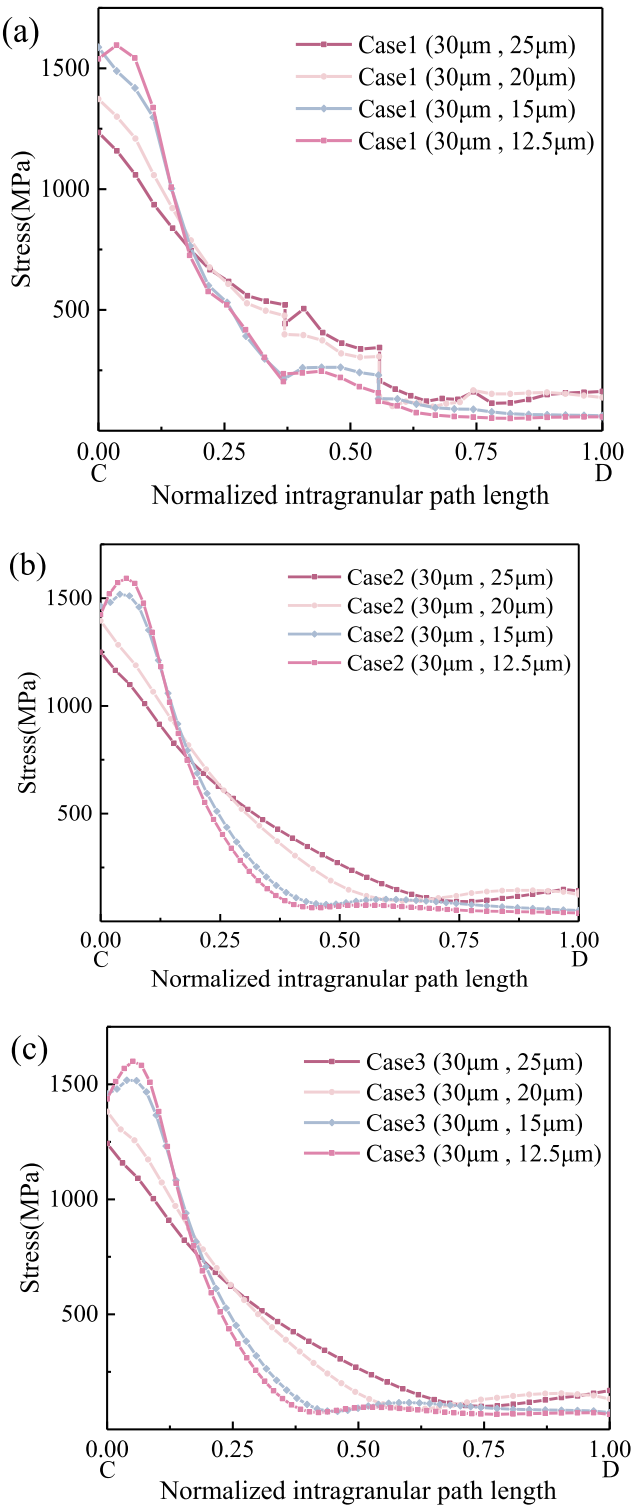

Fig. 8. Stress distribution along intragranular path (a) Case 1 with different aspect ratios; (b) Cases 2 with different aspect ratios; (c) Cases 3 with different aspect ratios.

distribution is to highlight the coordinated lamellar microstructural effect around microdefect such as the elliptical notch in the present work.

Determination of CPFEM modelling parameters for bimodal Ti-6Al-4V significantly affects the numerical results. Modelling parameters have been validated in [27,37]. Moreover, we have verified parameters related to β phase from [40,58]. They are tabulated in Table 1. In RVE modeling, microstructural features such as average grain size and α and β phase proportion are based upon corresponding experiments and statistics [27,49,58].

2.3. Intragrain weight integration approach

In bimodal Ti-6Al-4V titanium alloys, through the process of fatigue, cyclic loading results in localized strain in the form of slip bands. PSBs indicate localization of plastic deformation, slip and dislocations,

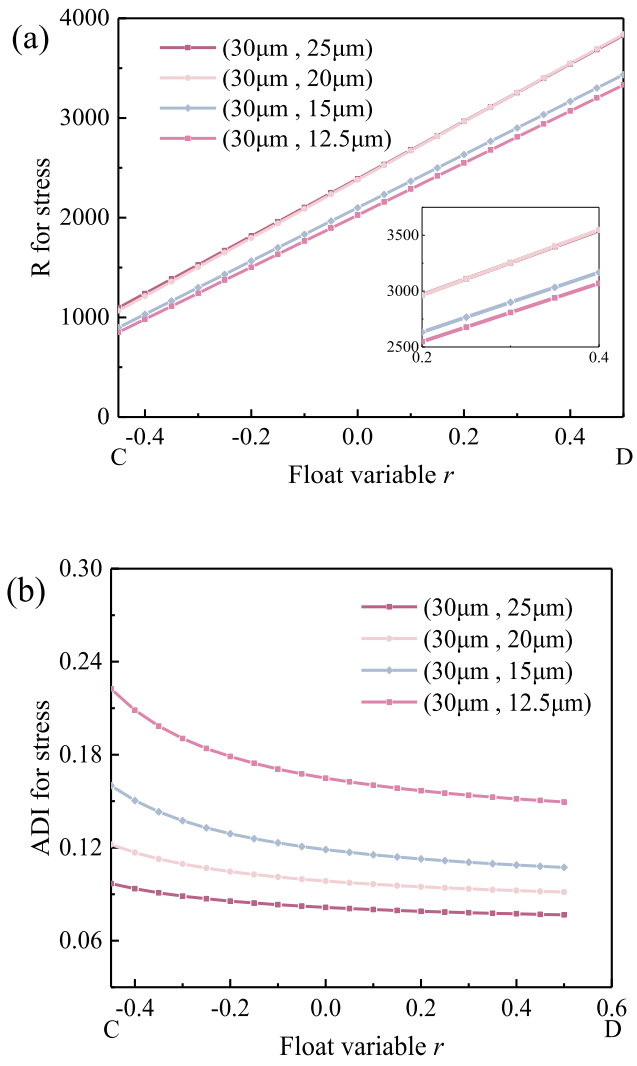

Fig. 9. Lamellar microstructural effect; (a) Intragrain weight integration for stress; (b) ADI for stress.

further leads to crack initiation [57]. PSBs can be found in primary α phase or LM. Preferred site for crack initiation is usually the interface between PSB and matrix. More specifically, crack nucleation can be either found in LM, primary α phase or the interface between primary α phase and lamellar matrix. Herein, we are mainly focused on the LM.

The first step is to identify critical location around the elliptical notch. Strain contour for the three cases are displayed in Fig. 2(a). Severe strain is observed in grains neighboring notch edge, with or without LM. Circular strain distribution after 10 cycles along the notch edge from A to B is presented in Fig. 2(b). Not surprisingly, peak of strain occurs near the left end of elliptical notch. This is described as critical location herein. Obvious oscillation of curve for Case I is observed for lamellar microstructural effect. If we focus on the single grain in critical location, Fig. 2(c) further illustrates the strain distribution along the intragranular path length from C to D. It is clearly observed these curves start at highest point from the left, decreasing gradually along intragranular path length. However, it is noticed that oscillations of curve for Case 1 with LM appear in the middle range, which is different from Case 2 and Case 3 for grains without LM.

In order to quantify the lamellar microstructural effect at critical location, an intragrain weight integration approach is proposed here to account for the effect of accumulated deformation within single grain. Considering the PSBs that contribute to crack initiation within grains, the main purpose of the intragrain weight integration approach is to stand out the accumulated deformation in single grain, and to study how it further affects the following fatigue crack initiation.

It shall be kept in mind that our endeavor is to focus on the lamellar microstructural effect on fatigue performance of bimodal Ti-6Al-4V titanium alloys with microdefect. As a case in point, one single grain at critical location neighboring microdefect is designated and LM distribution is tailored, as depicted in Fig. 3(a).

The intragranular path CD, as outlined in Fig. 3(b), is defined as grain length along the long axis of elliptical notch. In order to accommodate the abrupt deformation of one specific point within single grain, we consider the accumulated deformation as single value after integration along the intragranular path CD. Values of strain, stress and cumulative plastic slip along CD are extracted independently after unloading. Subsequently, a weight function $\psi(x)$ is tentatively proposed to reflect the contribution of various intragranular areas. Weighted value for the middle region ranging from $0.25\,l$ to $0.75l$ is set to be 1, while both ends of CD may adopt lower values of m with linear slope of k, refer to Fig. 3(c). The adjustment is to emphasize the contribution of middle region within grain. The formula is tentatively proposed as follows:

$$\psi(x) = \begin{cases} m + kx, & x \in (0, 0.25l) \\ 1, & x \in (0.25l, 0.75l) \\ m + k - kx, & x \in (0.75l, l) \end{cases} \tag{8}$$

A dimensionless parameter of float variable r is further defined such that the contribution of intragranular area can be correspondingly tailored, subsequently the updated weight function can be expressed as follows:

$$\hbar(x) = \psi(x) + r, r \in (-0.45, 0.5) \tag{9}$$

Thus, the intragrain weight integration on strain, stress and cumulative plastic slip along the intragranular path is defined as:

$$\mathrm{R} = \int \hbar(x)\Re \mathrm{d}x \tag{10}$$

$\Re$ is the individual values of strain/stress/cumulative plastic slip along the intragranular path. Denote R_1 as the weighted cumulative integration for grain with LM, R_0 as the weighted cumulative integration for grain without LM. Lamellar microstructural effect on the deformation thus is relatively quantified through the following equation:

$$\delta = \frac{\mathrm{R}_1 - \mathrm{R}_0}{\mathrm{R}_0} \tag{11}$$

Herein δ is the accumulative difference indicator (ADI) for strain/stress/cumulative plastic slip that relatively quantifies the lamellar microstructural effect. R is the corresponding weighted cumulative integration for the designated grain. LM effect will be graphically elaborated in the following results.

3. Results and discussions

3.1. Mesh sensitivity analysis

Computational efficiency and accuracy shall be balanced in CPFEM modelling. We take gradient mesh strategy in the present work. Very fine mesh size is employed around the microdefect, while relatively coarse mesh size is adopted afar. Considering LM is particularly focused here, we employ the three cases displayed in Fig. 1(b), 1(c) and 1(d) to perform mesh sensitivity analysis. Case 1 is focused on grain with LM distribution on the left edge of notch, while Cases 2 and 3 present grains without LM distribution in the critical location. Mesh sizes employed in critical location are 0.5 μm, 0.25 μm, and 0.1 μm. Stress values along the intragranular path are extracted and further presented in Fig. 4.

Displayed in Fig. 4(a) is the stress distribution along intragranular path for Case 1. Numerical results are fairly close when mesh sizes of 0.25 μm, and 0.1 μm are adopted. It is not surprising to notice that the curve for 0.5 μm deviates distinctly compared to the other two curves,

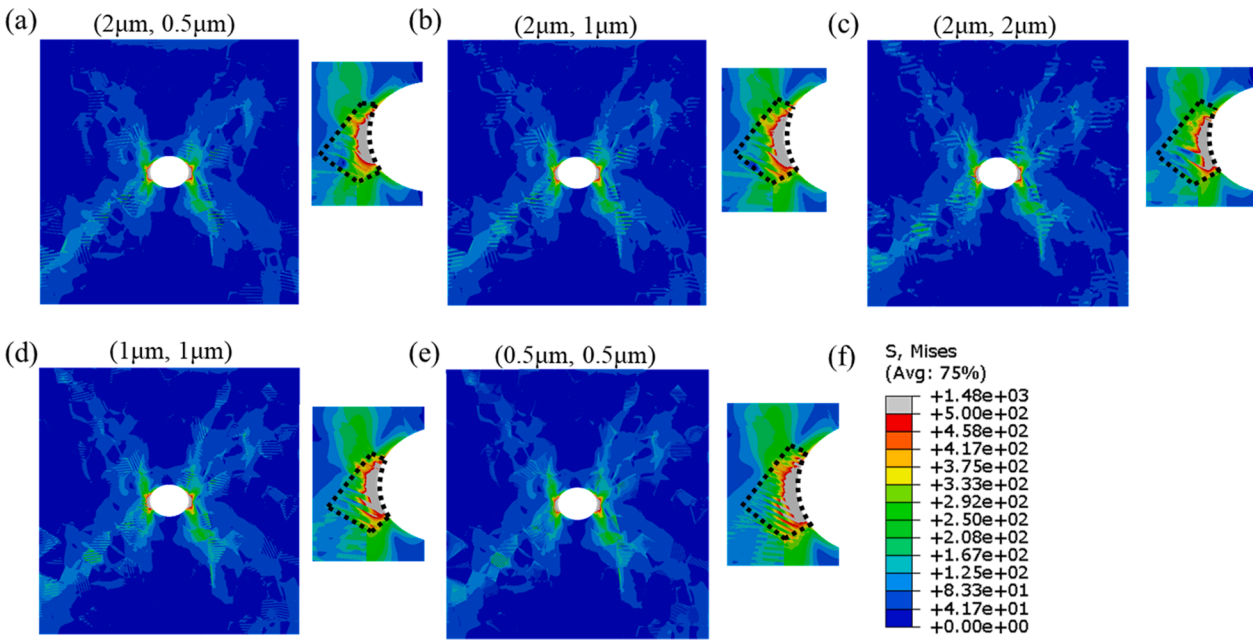

Fig. 10. Contour plot for lamellae with various combination of α phase and β phase lath thickness.

since relatively finer mesh size is necessitated in the modelling of lamellae consisting of secondary α and β laths. This is further evidenced by the three similar curves with the same three sets of mesh sizes, presented in Fig. 4(b) and 4(c) for Case 2 and Case 3. These numerical values extracted from grains without LM are less sensitive to mesh size, compared to Case 1 with LM.

Considering computational efficiency and accuracy, mesh size of 0.25 μm is adopted to perform the following CPFEM modelling.

3.2. Intragrain weight integration analysis

Based on mesh sensitivity analysis, mesh size of 0.25 μm is employed. After the cyclic loading, values of strain/stress/cumulative plastic slip are extracted along intragranular path and presented in Fig. 5. Trend of curves for strain/stress/cumulative plastic slip are generally consistent, decreasing monotonically from notch edge to afar. It is noticeable in Fig. 5(a) that curve of strain distribution in grain with LM oscillates appreciably in the middle range. Similar phenomenon can also be observed in Fig. 5(b) and 5(c), but in slightly different fashion. Both secondary α phase and β phase in lamellae are alternatively arranged, which is reflected through the high strain and relatively low stress for α phase, compared to the low strain and high stress for β phase. The oscillating curve falls exactly within the β phase range as depicted in Fig. 3(b). These numerical results are consistent with the existing findings in reference [44,58]. In a general sense, strain/stress redistribution along the intragranular path takes place in Case 1, compared to the smooth curves for Case 2 and Case 3. Oscillating curves of stress/strain occurs at middle range as well as the notch edge, as also experimentally evidenced in reference [21], that redistribution of intragranular strain in LM could possibly lead to the improvement of fatigue performance. This is interpreted as the increase of effective microstructural size in lamellae which further affects the early stage of fatigue crack initiation and propagation.

By combining Eqs. (8)-(10), intragrain weight integration on strain/stress/cumulative plastic slip along the intragranular path are carried out to achieve accumulated strain/stress/ cumulative plastic slip. Weighted cumulative integration R on strain/stress/cumulative plastic slip for designated grain are generated by use of Eq. (10), refer to Fig. 6. Note that the empirical parameters m and k are taken as 0.5 and 2, respectively. This is a trial and error process to highlight the contribution along the intragranular path. Schematically illustrated in Fig. 6 are the weighted cumulative integration R for strain/stress/cumulative plastic slip. Float variable r ranges from −0.45 to 0.5, indicating the varying contribution of different intragranular areas.

R for stress and strain are linearly increasing over the range of float variable. Difference between grain with LM (Case 1) and grains without LM (Cases 2 and 3) are gradually expanding, while the two curves for grains without LM are slightly different. Lamellar microstructural effect is relatively more influential compared to the factor of neighboring grains, which is distinctly indicated by the disparate curves of R for stress and strain.

It is also noticed in Fig. 6(c) that weighted cumulative integration on cumulative plastic slip differentiating Case 1 from Case 2 and Case 3 is less appreciable. Three curves are mostly overlapped. Thus, in what follows, we take weighted cumulative integration on strain and stress to quantify the lamellar microstructural effect in a variety of designed cases.

3.3. Microdefect size effect

Microdefect size has significant influence on the deformation around defect edges [50]. With the increase of length/height ratio, the elliptical notch could evolve indefinitely into an ideal line crack. In this section, we are focused on the three cases depicted in Fig. 1(b), 1(c) and 1(d). 4 sets of elliptical notches are defined, with the size of ($2a$, $2b$) assigned to be (30 μm, 25 μm), (30 μm, 20 μm), (30 μm, 15 μm) and (30 μm, 12.5 μm), respectively. Notch is tailored to be increasingly sharper such that the coordinated effect of microdefect and LM is studied.

Strain distribution along the intragranular path is graphically displayed in Fig. 7(a), 7(b) and 7(c), corresponding to Cases 1, 2 and 3, respectively. For the grain with LM distribution, curves oscillate appreciably at middle range due to lamellar microstructural effect. With the decrease of height, the elliptical notch becomes sharper. Thus, not surprisingly, strain deformation at notch edge increases noticeably. Strain concentration is more prominent for (30 μm, 12.5 μm), curve oscillates less compared to the other three sets of elliptical notches. It seems that positive lamellar microstructural effect on intragranular grain distribution is reducing for relatively sharper elliptical notch. Similar trend can be seen in Fig. 7(b) and 7(c), though the oscillating range induced by LM in Case 1 is missing. However, compared to Cases 2

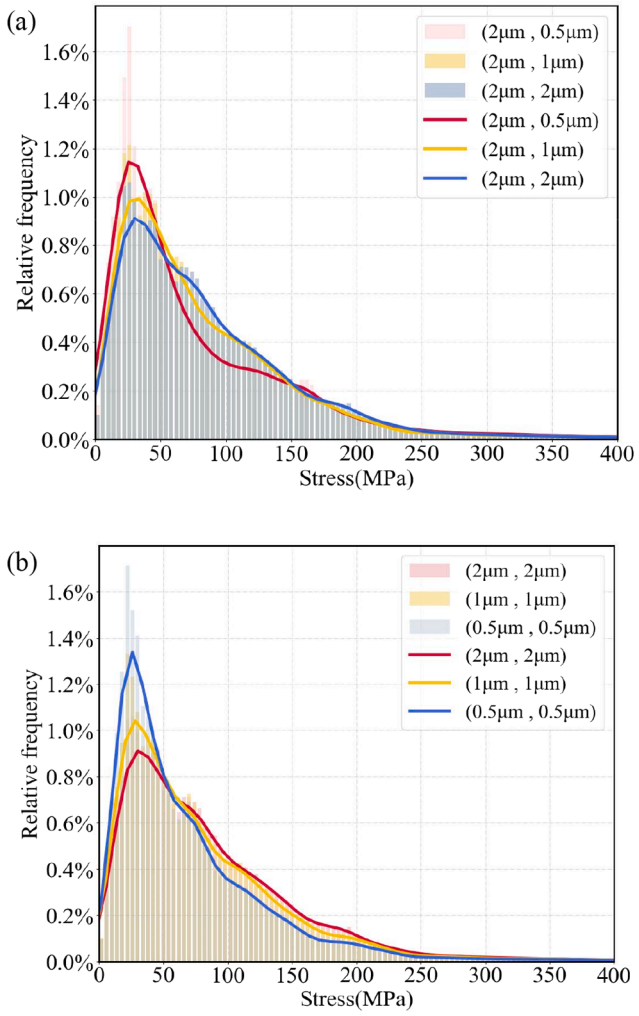

Fig. 11. Statistical stress distribution in RVEs for different combination of α and β lath thickness; (a) Increase of β lath thickness; (b) Synchronized refinement of both α and β lath thickness.

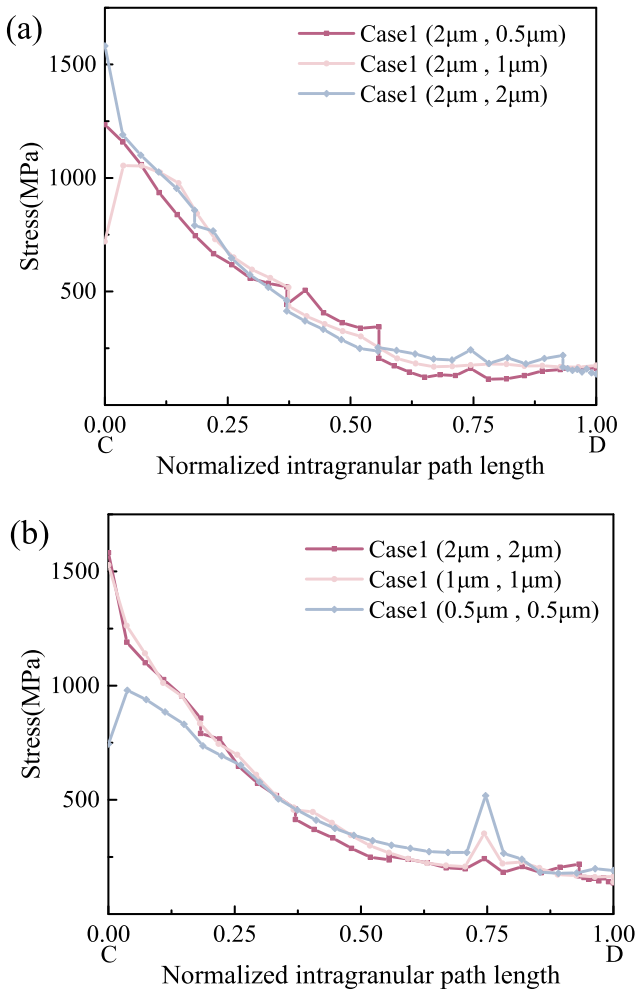

Fig. 12. Stress distribution along intragranular path (a) Case 1 with the increase of β lath thickness; (b) Case 1 with the synchronized refinement of α and β lath thickness.

and 3, under the influence of LM, strain deformation at notch edge in Case 1 is visibly quantitatively alleviated.

Subsequently, stress distribution along the intragranular path for Cases 1, 2 and 3 is illustrated with different length/height ratios, refer to Fig. 8. Similar to strain distribution, prominent stress concentration is observed at the edge of elliptical notch. Curve oscillation caused by LM is captured in Case 1, refer to Fig. 8(a).

Overall, curve trend of intragranular stress distribution is consistent with that in Fig. 7(a), 7(b) and 7(c). Lamellar microstructural effect in Case 1 is indicated through curve oscillation. However, quantifying the effect of LM is yet to be elaborated.

Intragrain weight integration on stress is carried out for Case 1 grain with LM. Graphically displayed in Fig. 9 is the presentation of lamellar microstructural effect via intragrain weight integration and ADI analysis. With the increase of float variable *r*, curves of intragrain weight integration on stress tend to be monotonically increasing. Disparities among the curves are appreciable, refer to Fig. 9(a). Variation of lamellar microstructural effect over the variation of notch size is clearly differentiated. Furthermore, we introduce the ADI defined for stress to quantify the lamellar microstructural effect. Difference of ADI curves between (30 μm, 25 μm) and (30 μm, 12.5 μm) tend to be disparately enlarged. With the increase of float variable *r*, the four sets of ADI values tend to be constantly stable. Based on the definition of ADI, notch with the length/height (30 μm, 12.5 μm) so far has the most prominent lamellar microstructural effect. The positive role of LM in materials and components with inevitable sharp defects cannot be overemphasized. Tailoring LM distribution around notch significantly affects the fatigue performance of materials and critical components.

3.4. Lamellae width effect

Lamellae consists of secondary α phase, as well as β phase. In previous sections, both α phase and β phase play significant role in intragranular deformation. In this section, lamellae width effect is studied in conjunction with the approach of quantifying the effect of LM. Based on collected statistical data [27,37], we assume the mean thickness of α lath to be 2 μm, the mean thickness of β lath to be 0.5 μm, denoted as (2 μm, 0.5 μm). Variation of lamellae width leads to 5 sets of combination, (2 μm, 0.5 μm), (2 μm, 1 μm), (2 μm, 2 μm), (1 μm, 1 μm) and (0.5 μm, 0.5 μm), sequenced by the increase of β lath thickness, as well as the synchronized refinement of both secondary α lath and β lath thickness.

Contour plots of stress distribution for the lamellae are graphically presented in Fig. 10. The overall appearance of contour plots displays fairly similar pattern of stress distribution, but visually varies in details. Within the designated grain, stress distribution varies noticeably. More surprisingly, increase of β lath thickness within the designated grain even further affect the stress distribution afar. The synchronized refinement of both α and β lath thickness also delicately transforms the general contour plot of stress distribution. We further present the statistical stress distribution in RVEs, for various combination of α and β

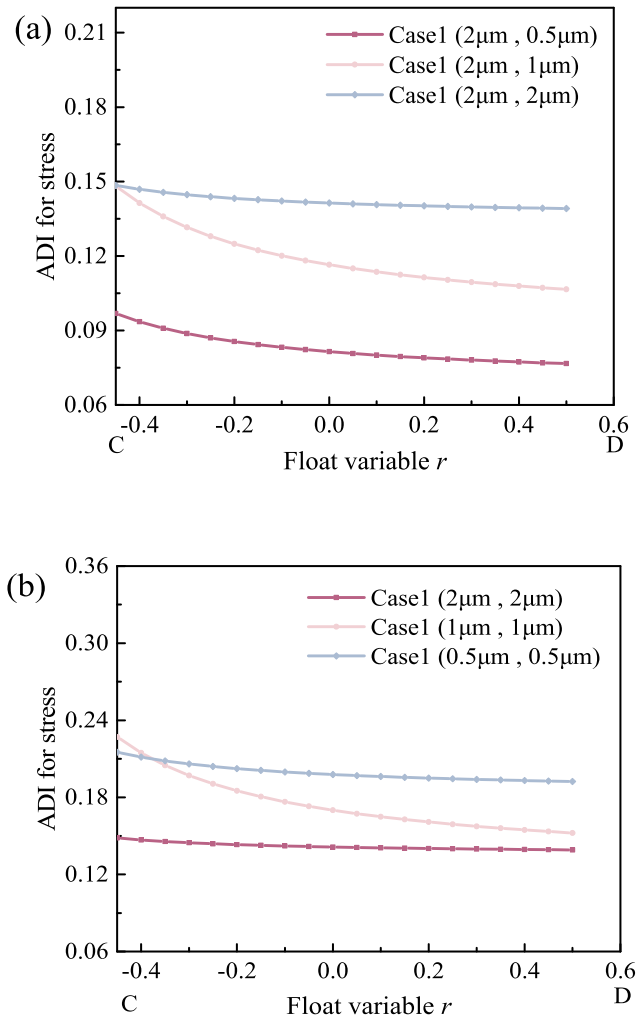

Fig. 13. Lamellar microstructural effect; (a) ADI for stress with the increase of β lath thickness; (b) ADI for stress with synchronized refinement of α and β lath thickness.

lath thickness, refer to Fig. 11. The high relative frequency corresponding to low level of stress approximately 25 MPa stands out in Fig. 1 (a), indicating the stress redistribution over the refinement of β lath thickness. Similar pattern of stress redistribution is also observed in the synchronized refinement of α and β lath thickness.

Conclusively, lamellar microstructural effect can be appreciably enhanced through the synchronized refinement of lamellae width, on the basis of contour plots in Fig. 10, as well as the statistical stress distribution in Fig. 11(b).

Curves generated from the variation of secondary α and β lath thickness in lamellae are displayed in Fig. 12. Lamellar microstructural effect on the fatigue behaviors is reflected through the curve oscillation that is not captured in grain without lamellae. With the increase of β lath thickness, Curve of intragranular stress distribution oscillate in an appreciable fashion, while stress at notch edge does not vary in a sequenced order. However, synchronized refinement of α and β lath thickness display distinct stress drop at notch edge, and oscillate appreciably through the curve range. Notice the combination of (0.5 μm, 0.5 μm) represent finer thickness of both α and β laths, and demonstrate the relatively ideal intragranular stress distribution, compared to the other two sets. We further perform ADI analysis on quantifying lamellar microstructural effect, refer to Fig. 13.

ADI analysis offers a straightforward yet distinct perspective on lamellar microstructural effect. Level of ADI for stress in Fig. 13(a) are disparate, over the variation of β lath thickness. The highest level of lamellar microstructural effect is observed for the β lath thickness of 2 μm. For the combination of (2 μm, 2 μm), due to the lower stiffness in α phase, β phase is expected to undertake more relatively high stress, as evidenced by the blue curve displayed in Fig. 11(a). Synchronized refinement of α and β lath thickness turns out to be monotonically increasing the level of ADI defined for stress, interpreted as the more prominent lamellar microstructural effect. Similar findings in [44] suggest that the refinement of α_s lath thickness plays a positive role of improving fatigue performance of Ti-6Al-4V. It is also concluded in [27] that thinner lamellae width results in the lowest probability of fatigue crack formation for Ti-6Al-4V. These experimental and numerical results are a qualitative testament to the effectiveness and credibility of our proposed approach.

4. Concluding remarks

Within the framework of CPFEM, the present work has brought coordinated microdefect and neighboring lamellar microstructural effects on fatigue performance of bimodal Ti-6Al-4V to in-depth investigation. Numerically tailoring LM distribution around microdefect is made feasible, avoiding the difficulties and challenges experimental procedure is short of. We propose an intragrain weight integration approach to account for the intragranular deformation, to highlight the contribution of various intragranular areas. The defined ADI for stress is able to relatively quantify lamellar microstructural effect. Mesh sensitivity analysis, intragrain weight integration approach, microdefect size effect, as well as lamellae width effect, are systematically investigated. Main findings are summarized as follows:

The defined ADI for stress, as well as intragrain weight integration approach, effectively quantifies lamellar microstructural effect, and is able to differentiate lamellar structure from nonlamellar structures under fatigue.

With the increase of length/height ratio, stress/strain concentration effects intensify at notch edge. However, values of ADI that reflects lamellar microstructural effect is appreciably improved. Fatigue performance of defected bimodal titanium alloys shall be closely associated with lamellar structures.

Decrease of secondary α_s lath thickness, as well as increase of β lath thickness, results in the improvement of lamellar microstructural effect. Synchronized refinement of LM also improves the level of lamellar microstructural effect.

Last but not least, at this stage, we are primarily focused on the designated grain with LM at critical location. Under fatigue loading, interaction between designated grain and neighboring grains is more complex and challenging. The proposed intragrain weight integration approach, as well as defined ADI, offers a unique perspective on quantifying lamellar microstructural effect, yet remain to be further completed in the forthcoming work.

Declaration of Competing Interest

The authors declare that they have no known competing financial interests or personal relationships that could have appeared to influence the work reported in this paper.

Data Availability Statement.

The data that support the findings of this study are available from the corresponding author upon reasonable request.

Acknowledgements

KT and KC acknowledge the financial support from National Natural Science Foundation of China (NSFC) under grant number 11872278, as well as Science and Technology Commission of Shanghai Municipality (STCSM) under grant number 21ZR1467200.

References

[1] Wilson D, Wan W, Dunne FP. Microstructurally-sensitive fatigue crack growth in HCP, BCC and FCC polycrystals. J Mech Phys Solids 2019;126:204–25.
[2] Wu GQ, Shi CL, Sha W, Sha AX, Jiang HR. Effect of microstructure on the fatigue properties of Ti–6Al–4V titanium alloys. Mater Des 2013;46:668–74.
[3] Tang K, Chen K, Ferro P, Berto F. Tuning lamellar structure distribution around elliptical notch in Ti-6Al-4V for fatigue performance. Proc Struct Integrity 2022;39:387–92.
[4] Romero C, Yang F, Bolzoni L. Fatigue and fracture properties of Ti alloys from powder-based processes–A review. Int J Fatigue 2018;117:407–19.
[5] Campanelli LC. A review on the recent advances concerning the fatigue performance of titanium alloys for orthopedic applications. J Mater Res 2021;36(1):151–65.
[6] Lütjering G, Williams JC. Titanium. Springer Science & Business Media; 2007.
[7] Hall JA. Fatigue crack initiation in α-β titanium alloys. Int J Fatigue 1997;19(93):23–37.
[8] Zhang T, Liu C-T. Design of titanium alloys by additive manufacturing: A critical review. Adv Powder Mater 2022;1(1):100014.
[9] Zhang W, Hu Y, Ma X, Qian G, Zhang J, Yang Z, et al. Very-high-cycle fatigue behavior of AlSi10Mg manufactured by selected laser melting: Crystal plasticity modeling. Int J Fatigue 2021;145:106109.
[10] Asim UB, Siddiq MA, Kartal ME. A CPFEM based study to understand the void growth in high strength dual-phase titanium alloy (Ti-10V-2Fe-3Al). Int J Plast 2019;122:188–211.
[11] Yuan G-J, Wang R-Z, Gong C-Y, Zhang X-C, Tu S-T. Investigations of micro-notch effect on small fatigue crack initiation behaviour in nickel-based alloy GH4169: Experiments and simulations. Int J Fatigue 2020;136:105578.
[12] Gaur V, Briffod F, Enoki M. Micro-mechanical investigation of fatigue behavior of Al alloys containing surface/superficial defects. Mater Sci Eng, A 2020;775:138958.
[13] Jiang W, Yao W, Li P, Luo P. A fatigue life prediction method distinguishing fracture modes for Ni-based single crystal superalloys considering porosity defect. Theor Appl Fract Mech 2021;112:102883.
[14] Nalla RK, Ritchie RO, Boyce BL, Campbell JP, Peters JO. Influence of microstructure on high-cycle fatigue of Ti-6Al-4V: Bimodal vs. lamellar structures. Metall Mater Trans A 2002;33(13):899–918.
[15] Cui Y, Li C, Zhang C, Li R, Ren Y, Zheng W, et al. Effect of initial microstructure on the micromechanical behavior of Ti-55531 titanium alloy investigated by in-situ high-energy X-ray diffraction. Mater Sci Eng, A 2020;772:138806.
[16] Yang C, Kang LM, Li XX, Zhang WW, Zhang DT, Fu ZQ, et al. Bimodal titanium alloys with ultrafine lamellar eutectic structure fabricated by semi-solid sintering. Acta Mater 2017;132:491–502.
[17] Jadhav S, Powar A, Patil S, Supare A, Farane B, Singh R. Effect of volume fraction of α and transformed β on the high cycle fatigue properties of bimodal Ti6Al4V alloy. InIOP Conference Series: Materials Science and Engineering 2017 (Vol. 201, No. 1, p. 012035). IOP Publishing.
[18] Zeng LR, Lei LM, Yang J, Luo XM, Zhang GP. Microstructure-Dependent Local Fatigue Cracking Resistance of Bimodal Ti–6Al–4V Alloys. Adv Eng Mater 2018;20(4):1700702.
[19] Wu D, Liu L, Zhang L, Wang W, Zhou K. Tensile deformation mechanism and micro-void nucleation of Ti-55531 alloy with bimodal microstructure. J Mater Res Technol 2020;9(6):15442–53.
[20] Zhang C, Hu K, Zheng M, Zhu W, Song G. Effect of surface nanocrystallization on fatigue properties of Ti–6Al–4V alloys with bimodal and lamellar structure. Mater Sci Eng, A 2021;813:141142.
[21] Ren J, Wang Qi, Zhang B, Yang D, Lu X, Zhang X, et al. Influence of microstructure on fatigue crack growth behavior of Ti–6Al–3Nb–2Zr–1Mo alloy: Bimodal vs. lamellar structures. Intermetallics 2021;130.
[22] Wang Q, Ren J, Zhang B, Xin C, Wu Y, Ye M. Influence of microstructure on the fatigue crack growth behavior of a near-α TWIP Ti alloy. Mater Charact 2021;178:111208.
[23] Lei L, Zhao Q, Zhao Y, Huang S, Wu C, Jia W, et al. Study on the intrinsic factors determining impact toughness of TC21 alloy. Mater Charact 2021;177:111164.
[24] Zhang S, Tian N, Li D, Li J, Jin F, Wang G, et al. Microstructure evolution and fracture mechanism of a TiAl–Nb alloy during high-temperature tensile testing. Mater Sci Eng, A 2022;831:142094.
[25] Roy S, Suwas S. Orientation dependent spheroidization response and macro-zone formation during sub β-transus processing of Ti-6Al-4V alloy. Acta Mater 2017;134:283–301.
[26] Chen W, Zeng W, Xu J, Zhou D, Wang S, He S. Deformation behavior and microstructure evolution during hot working of Ti60 alloy with lamellar starting microstructure. J Alloy Compd 2019;792:389–98.
[27] Zhang M, Han F, Tang B, Kou H, Fan J, Li J. Effects of microstructure on high cycle fatigue properties of dual-phase Ti alloy: combined nonlocal CPFE simulations and extreme value statistics. J Mater Res Technol 2020 May;9(3):5991–6000.
[28] Jiang XQ, Fan XG, Zhan M, Wang R, Liang YF. Microstructure dependent strain localization during primary hot working of TA15 titanium alloy: Behavior and mechanism. Mater Des 2021;203:109589.
[29] Wang X, Li J, Ameyama K, Dirras G. Influence of microstructural features on the yield strength of Ti–6Al–4V: a numerical study by using the crystal plasticity finite element method. Meccanica 2021;56(5):1129–46.
[30] Campbell A, Murray P, Yakushina E, Marshall S, Ion W. New methods for automatic quantification of microstructural features using digital image processing. Mater Des 2018;141:395–406.
[31] Gong J, Wilkinson AJA. microcantilever investigation of size effect, solid-solution strengthening and second-phase strengthening for ⟨a⟩ prism slip in α-Ti. Acta Mater 2011;59(15):5970–81.
[32] Prithivirajan V, Sangid MD. Examining metrics for fatigue life predictions of additively manufactured IN718 via crystal plasticity modeling including the role of simulation volume and microstructural constraints. Mater Sci Eng, A 2020;783:139312.
[33] Briffod F, Shiraiwa T, Enoki M. Nucleation and propagation modeling of short fatigue crack in rolled bi-modal Ti–6Al–4V alloy. Mater Sci Eng, A 2020;790:139710.
[34] Muth A, John R, Pilchak A, Kalidindi SR, McDowell DL. Analysis of fatigue indicator parameters for ti-6al-4v microstructures using extreme value statistics in the 'HCF regime. Int J Fatigue 2021;145:106096.
[35] Li K-S, Wang R-Z, Yuan G-J, Zhu S-P, Zhang X-C, Tu S-T, et al. A crystal plasticity-based approach for creep-fatigue life prediction and damage evaluation in a nickel-based superalloy. Int J Fatigue 2021;143:106031.
[36] Bridier F, McDowell DL, Villechaise P, Mendez J. Crystal plasticity modeling of slip activity in Ti–6Al–4V under high cycle fatigue loading. Int J Plast 2009;25(6):1066–82.
[37] Han F, Tang B, Kou H, Li J, Feng Y. Experiments and crystal plasticity finite element simulations of nanoindentation on Ti–6Al–4V alloy. Mater Sci Eng, A 2015;625:28–35.
[38] Han F, Tang B, Kou H, Li J, Deng Y, Feng Y. Cyclic softening behavior of Ti–6Al–4V alloy at macro and micro-scale. Mater Lett 2016;185:115–8.
[39] Han F, Tang B, Yan X, Peng Y, Kou H, Li J, et al. Indentation pileup behavior of Ti-6Al-4V Alloy: experiments and nonlocal crystal plasticity finite element simulations. Metall Mater Trans A 2017;48(4):2051–61.
[40] Kapoor K, Yoo YS, Book TA, Kacher JP, Sangid MD. Incorporating grain-level residual stresses and validating a crystal plasticity model of a two-phase Ti-6Al-4 V alloy produced via additive manufacturing. J Mech Phys Solids 2018;121:447–62.
[41] Ferreri NC, Ghorbanpour S, Bhowmik S, Lussier R, Bicknell J, Patterson BM, et al. Effects of build orientation and heat treatment on the evolution of microstructure and mechanical properties of alloy Mar-M-509 fabricated via laser powder bed fusion. Int J Plast 2019;121:116–33.
[42] Roy U, McDowell DL, Zhou M. Effect of grain orientations on fracture behavior of polycrystalline metals. J Mech Phys Solids 2021;151:104384.
[43] Schnabel JE, Scheider I. Crystal plasticity modeling of creep in alloys with LMs at the example of fully lamellar TiAl. Front Mater 2021;581187.
[44] Geng Y, Harrison N. Functionally graded bimodal Ti6Al4V fabricated by powder bed fusion additive manufacturing: Crystal plasticity finite element modelling. Mater Sci Eng, A 2020;773:138736.
[45] Zhang J, Li H, Sun X, Zhan M. A multi-scale MCCPFEM framework: modeling of thermal interface grooving and deformation anisotropy of titanium alloy with lamellar colony. Int J Plast 2020;135:102804.
[46] Du Z, Tang K, Ferro P. Quantitative analyses on geometric shape effect of microdefect on fatigue accumulation in 316L stainless steel. Eng Fract Mech 2022;269:108517.
[47] Li L, Shen L, Proust G. Fatigue crack initiation life prediction for aluminium alloy 7075 using crystal plasticity finite element simulations. Mech Mater 2015;81:84–93.
[48] Jiang J, Yang J, Zhang T, Zou J, Wang Y, Dunne FP, et al. Microstructurally sensitive crack nucleation around inclusions in powder metallurgy nickel-based superalloys. Acta Mater 2016;117:333–44.
[49] Owolabi G, Okeyoyin O, Olasumboye A, Whitworth H. A new approach to estimating the fatigue notch factor of Ti-6Al-4V components. Int J Fatigue 2016;82:29–34.
[50] Guerchais R, Morel F, Saintier N. Effect of defect size and shape on the high-cycle fatigue behavior. Int J Fatigue 2017;100:530–9.
[51] Sausto F, Patriarca L, Foletti S, Beretta S, Vacchieri E. Strain Localizations in Notches for a Coarse-Grained Ni-Based Superalloy: Simulations and Experiments. Materials 2021;14(3):564.
[52] Tang K, Du Z, Ferro P, Berto F. Crack initiation and propagation from geometric microdefects: Experiment and transition fatigue behavior. Fatigue Fract Eng Mater Struct 2021;44(9):107132.
[53] Huang Y. A user-material subroutine incorporating single crystal plasticity in the ABAQUS finite element program. Cambridge: Harvard University, 1991.
[54] Asaro RJ, Rice JR. Strain localization in ductile single crystals. J Mech Phys Solids 1977;25(3):309–38.
[55] Hutchinson JW. Creep and plasticity of hexagonal polycrystals as related to single crystal slip. Metall Trans A 1977;8(9):1465–9.
[56] Asaro RJ. Micromechanics of crystals and polycrystals. Adv Appl Mech 1983;23:1–115.
[57] Sangid MD, Maier HJ, Sehitoglu H. A physically based fatigue model for prediction of crack initiation from persistent slip bands in polycrystals. Acta Mater 2011;59(1):328–41.
[58] Kapoor K, Raui P, Noraas R, et al. Modeling Ti-6Al-4V using crystal plasticity, calibrated with multi-scale experiments, to understand the effect of the orientation and morphology of the alpha and beta phases on time dependent cyclic loading. J Mech Phys Solids 2021;146:104192.